

The role of images and priors in measuring H_0 from supernova Refsdal in galaxy cluster MACS J1149.5+2223

Liliya L.R. Williams,¹★ Jori Liesenborgs²

¹*School of Physics and Astronomy, University of Minnesota, 116 Church Street, Minneapolis, MN 55455, USA*

²*UHasselt - tUL, Expertisecentrum voor Digitale Media, Wetenschapspark 2, B-3590, Diepenbeek, Belgium*

Accepted XXX. Received YYY; in original form ZZZ

ABSTRACT

Multiple image gravitational lensing systems with measured time delays provide a promising one-step method for determining H_0 . MACS J1149, which lenses SN Refsdal into a quad S1-S4, and two other widely separated images, SX and SY, is a perfect candidate. If time delays are pinned down, the remaining uncertainty arises from the mass distribution in the lens. In MACS J1149, the mass in the relevant lens plane region can be constrained by many multiple images, the mass of the galaxy splitting S1-S4 (which, we show, is correlated with H_0), magnification of SX (also correlated with H_0), and prior assumptions on the mass distribution. To better understand what affects the measurement of H_0 , we separate out the uncertainties associated with these constraints. Using images alone yields $\sim 1000\%$ uncertainty, despite the fact that the position of SX is recovered to within $\sim 0.04''$ (rms $\sim 0.26''$) by GRALE lens inversion. Fixing the mass of the galaxy that splits S1-S4 would reduce 1σ uncertainties to 20%–33%, depending on the mass, while fixing the magnification of SX would reduce 1σ uncertainties to 35%. Smaller uncertainties, of order few percent, are a consequence of imposing assumptions on the shapes of the galaxy and cluster mass distributions, which may or may not apply in a highly non-equilibrium environment of a merging cluster. We propose that if a measurement of H_0 is to be considered reliable, it must be supported by a wide range of lens inversion methods.

Key words: gravitational lensing: strong – dark matter – galaxies: clusters: individual: MACS J1149.5+2223

1 INTRODUCTION

Multiple image gravitationally lensed systems can be used to measure H_0 in one step (Refsdal 1964), and completely independently of the distance ladder. The two inputs are the observed time delays between multiple images, and the mass distribution in the lens. In galaxy-size lenses, with quasars as sources, time delay measurements are currently uncertain at the few%–10% level (Bonvin et al. 2016, 2018; Courbin et al. 2018).

In galaxy clusters, with supernovae as sources, the uncertainty in time delay measurement can be reduced because clusters are large, and hence all scales, including time scales, get blown up, reducing the fractional errors in time delay measurements.

The first multiply imaged supernova (Kelly et al. 2015), nicknamed Refsdal, was discovered in Grism Lens Amplified Survey from Space (GLASS; PI T. Treu) as four quad

images, S1-S4, surrounding an elliptical galaxy, in the Hubble Frontier Field (HFF; PI J. Lotz) galaxy cluster MACS J1149.5+2223 (hereafter MACS J1149). Refsdal was later confirmed to be a supernova, of a type similar to that of SN 1987A (Kelly et al. 2016b). The time delays between all the images of the quad were measured to be a few days to 3-4 weeks (Rodney et al. 2016). Viewed on cluster scale, images S1-S4 form in the second lowest minimum of the arrival time surface. Based on mass models (Sharon & Johnson 2015; Diego et al. 2016; Grillo et al. 2016; Jauzac et al. 2016; Oguri 2015; Kawamata et al. 2016), a cluster-scale saddle-point image, SX, was predicted (Treu et al. 2016), and then observed (Kelly et al. 2016a), at the time and position consistent with predictions. These successes prompted early estimates of H_0 from Refsdal (Vega-Ferrero et al. 2018; Grillo et al. 2018). The same cluster also hosts a transient, arising from a highly magnified, macro- and micro-lensed, massive high-redshift star (Kelly et al. 2018), whose images, Icarus (LS1/Lev16A) and Iapyx (Lev16B), separated by $\sim 0.3''$, straddle a nearby portion of the cluster critical line. The

★ E-mail: llrw@umn.edu (LLRW)

supernova and the transient source live in the same, triply imaged, face-on spiral galaxy at $z = 1.489$. The whole system of lensed images in MACS J1149 is spectacular and unique, and needs as much detailed investigation as possible.

This host galaxy cluster at $z = 0.542$ was first identified as one of 12 most distant X-ray luminous clusters detected at $z > 0.5$ by the Massive Cluster Survey, MACS (Ebeling et al. 2007). It is a double merger (Golovich et al. 2016), and one of the most complex merging clusters known (Ogrea et al. 2016). It was observed with the Advanced Camera for Surveys on HST, and analyzed and modeled by Zitrin & Broadhurst (2009), Smith et al. (2009) and Rau et al. (2014). They found three images of an extended, and surprisingly undistorted background spiral at $z = 1.489$, which is also the host of both SN Refsdal and the transient.

The time delay between Refsdal images S1 and SX can be determined to a 1-2% precision (Kelly et al., in preparation). However, the mass distribution is an additional, and largest source of uncertainty. Several mass models reproduce the lensed images within observational uncertainties, but lensing degeneracies can prevent an accurate and precise determination of H_0 . Models that quote low uncertainties usually rely on lens inversion methods that break many degeneracies through the use of parametric mass distribution assumptions.

The goal of this paper is to investigate how much precision in H_0 is possible based solely on the lensed image positions, and relations implied by lensing reconstructions, and how much precision is brought about through the use of priors, i.e., the assumptions about the density profiles of cluster galaxies and cluster dark matter. We do this by comparing the precision achieved by free-form GRALE reconstructions, which are based on image positions only, and the precision yielded by parametric mass models, which use lensed images as well as priors on mass distribution. Such understanding of the error budget is important when striving at a precision level of a few percent in H_0 .

We adopt the concordance Λ CDM cosmological model: flat, matter density, $\Omega_m = 0.3$, cosmological constant density, $\Omega_\Lambda = 0.7$, and the dimensionless Hubble constant $h = 0.7$, such that $H_0 = 100h \text{ km s}^{-1} \text{ Mpc}^{-1}$. At the redshift of the cluster, $z_l = 0.542$, 1" translates into 6.36 kpc. The source galaxy of Refsdal is at $z_s = 1.489$, and the critical surface mass density for sources at that redshift is $\Sigma_{\text{crit}} = [c^2/(4\pi G)]D_{\text{os}}/(D_{\text{ol}}D_{\text{ls}}) = 0.496 \text{ g cm}^{-2}$, where D 's are the angular diameter distances between the observer, o , lens, l , and source, s . We express the projected surface mass density in the lens in units of Σ_{crit} , and denote that dimensionless quantity by κ .

2 GRALE-BASED INVERSIONS

2.1 Method & input

GRALE is a flexible, free-form, adaptive grid lens inversion method, based on a genetic algorithm. It has been described extensively in previous works (Liesenborgs et al. 2006, 2007; Mohammed et al. 2014; Meneghetti et al. 2017). Here, we give a brief summary. A GRALE run starts with an initial coarse uniform grid in the lens plane populated with a basis set, such as projected Plummer density spheres (Plummer

1911). Each grid cell has a single Plummer sphere, with the size matching the cell size. Plummer spheres are chosen because they have constant central density, and rapidly, but smoothly falling off density at larger radii. As the code runs, the denser regions are resolved with a finer grid, with each cell given a Plummer with a proportional width. The initial trial solution, as well as all later evolved solutions are evaluated for genetic fitness, and the fit ones are cloned, combined and mutated. The final map consists of a superposition of many Plummers, typically several hundred to a couple of thousand, each with its own size and weight, determined by the genetic algorithm. Note that there is no one-to-one correspondence between Plummer spheres and astrophysical mass concentrations, like cluster-wide dark matter distributions, or individual galaxies. Plummer spheres are building blocks of these structures.

For this paper, GRALE uses a combination of two types of fitness measures: based on (i) image positions, and (ii) the null space. (i) Images are assumed to be point-like in this version of GRALE, and to assign this fitness measure the observed point images are first projected back onto their source planes. If the points of the same sources lie closer together, the trial solution is considered to have a better fitness value. The distances between the points are not measured on an absolute scale however. Instead, the size of the area of all backprojected points (of all sources) is used as a length scale. This helps avoid mass-sheet degenerate solutions (see below) having the advantage by introducing a relatively large mass-sheet component, as this would project all image points onto a smaller area. (ii) A trial solution under consideration may perform well regarding fitness measure (i), but still predict unobserved additional images. To take this into account, an area that is larger than the region of the observed images is subdivided into a grid of triangles. By counting the number of backprojected triangles that overlap with the envelope of the backprojected image points, trial solutions can be penalized if they predicted additional images.

We used the following as input to our models: positions of all 93 multiple images of knots in the spiral source galaxy from Table 4 of Treu et al. (2016), and positions of the 4 Refsdal S1-S4 images. All these are at $z = 1.489$. Estimating source redshifts using lens inversion techniques can lead to biased estimates, because of lensing degeneracies (Williams et al. 2017). To avoid that we used 20 images that had spectroscopic redshifts (also from Treu et al. 2016). For sources at very high redshifts, the uncertainties in redshifts become less important; the fractional change in Σ_{crit} between $z_s = 2$ and 4 is 0.164, while between $z_s = 4.5$ and 6.5 it is 0.041, i.e., four times smaller. To supplement our image set, we included two sources (6 images) with photometric redshifts of 4.8 and 6.5, respectively. In all, we used 123 images from 40 sources. These image data presented in Treu et al. (2016) were based on spectroscopic redshifts from VLT-MUSE (Grillo et al. 2016), Keck DEIMOS and HST-WFC3 (Brammer et al. 2016; Wang et al. 2017; Treu et al. 2015). The images we used are shown in Figure 1.

Treu et al. (2016) and Kelly et al. (2016a) present results of several lens inversion models, predicting, in advance of the event, the location and arrival time of Refsdal image at SX, which was first detected on December 11, 2015. In order to directly compare our results to the published ones, we did not use the observed position of SX as a constraint.

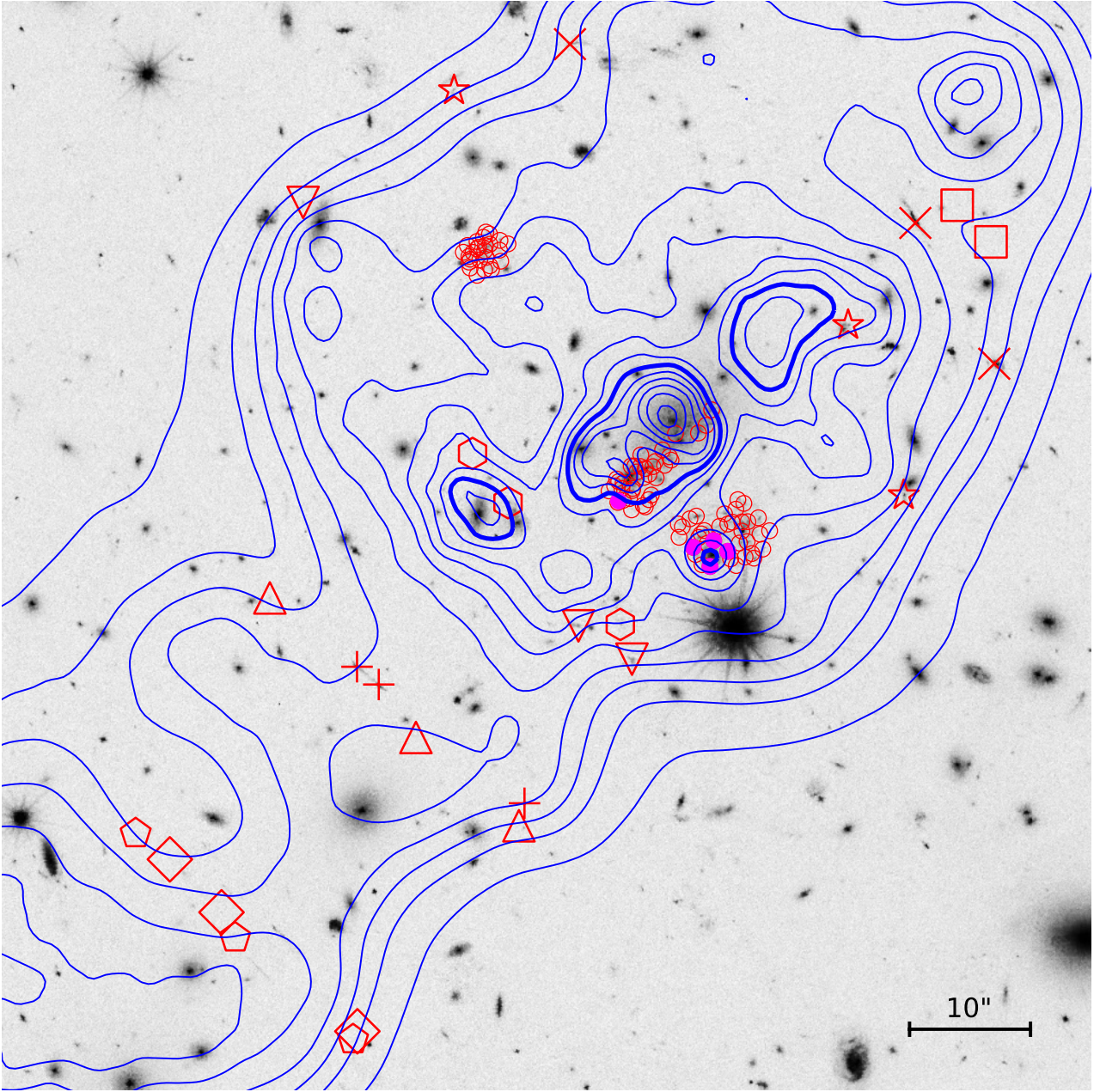


Figure 1. Multiple images used in this work (red symbols) are superimposed on an HST image of MACS J1149. Same symbol types identify images belonging to the same source. Three sets of about 33 empty circles are the knots of the spiral galaxy at $z_s = 1.489$. Magenta solid dots show the quad S1-S4 and SX image of supernova Refsdal. The projected isodensity contours of the HighResolution maps, at intervals of $\delta\kappa = 0.1$ (for $z_s = 1.489$), are shown in blue, with the thick contour representing $\kappa = 1$. The $10''$ length scale shown in the figure corresponds to 63.6 kpc at the redshift of the cluster, $z_l = 0.542$.

We also did not include the observed positions of the two transients, Icarus and Iapyx, as these had not yet appeared at the time of the published predictions. As all previous GRALE reconstructions, and in contrast to all but one other existing technique (Quinn Finney et al. 2018), our models do not use any information about galaxies in the lens or along the line of sight.

2.2 Inversion results

Each GRALE run consists of 9 sequential solutions, where the number of Plummets, and hence mass resolution, increases with each subsequent solution. We carry out a total of 75 of these runs¹, each of which is started with its own random

¹ These reconstructions are not the same as the v.4 set submitted to HST in early 2017. The v.4 reconstructions did not include S1-S4, and had a somewhat different, and smaller input image set.

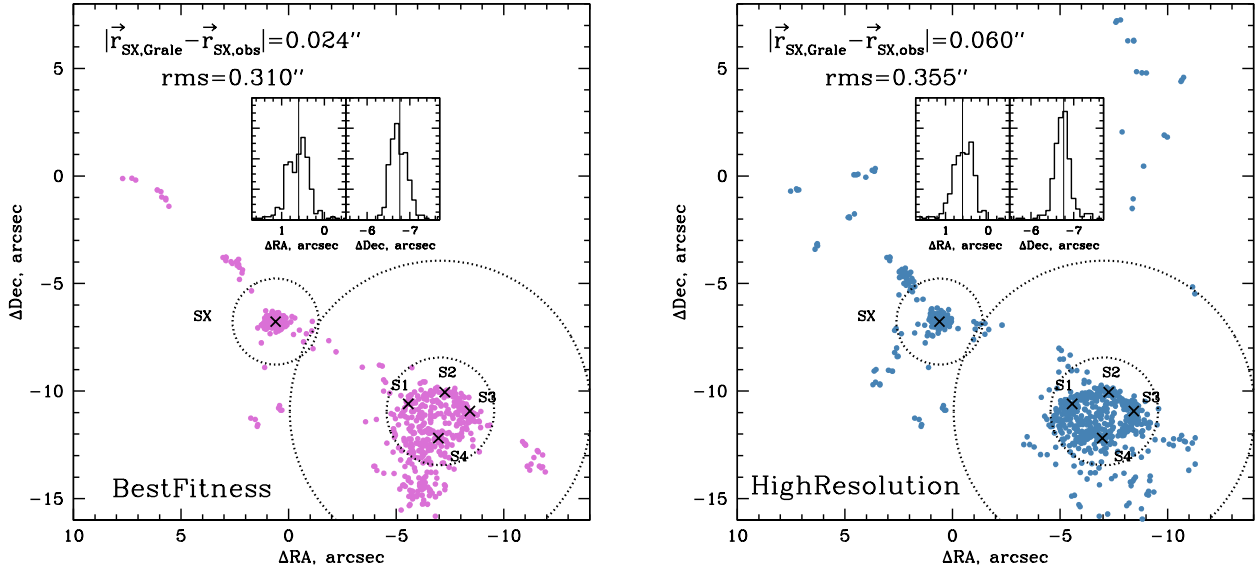


Figure 2. *Left:* The points are all the images of Refsdal predicted by the BestFitness set of GRALE mass maps from 75 independent runs. To obtain these, each of the observed S1-S4 images was traced back to the source plane, and used individually as sources to generate predicted images. The total number of images is over 1000. The observed SX, S1-S4 are marked with black crosses. The images within the black dotted circle of radius $2''$ around SX were used to calculate the average location and the rms of the predicted SX (displayed in the figure). The insets show the distribution of the ΔRA and ΔDec of predicted SX images. Vertical lines mark the observed values. The black dotted circles around S1-S4, of radii $2.5''$ and $7''$, are used to select reconstructions for the BFsubset; see Section 3 for details. *Right:* Same as the left panel, but for the HighResolution set of GRALE maps from the same 75 runs.

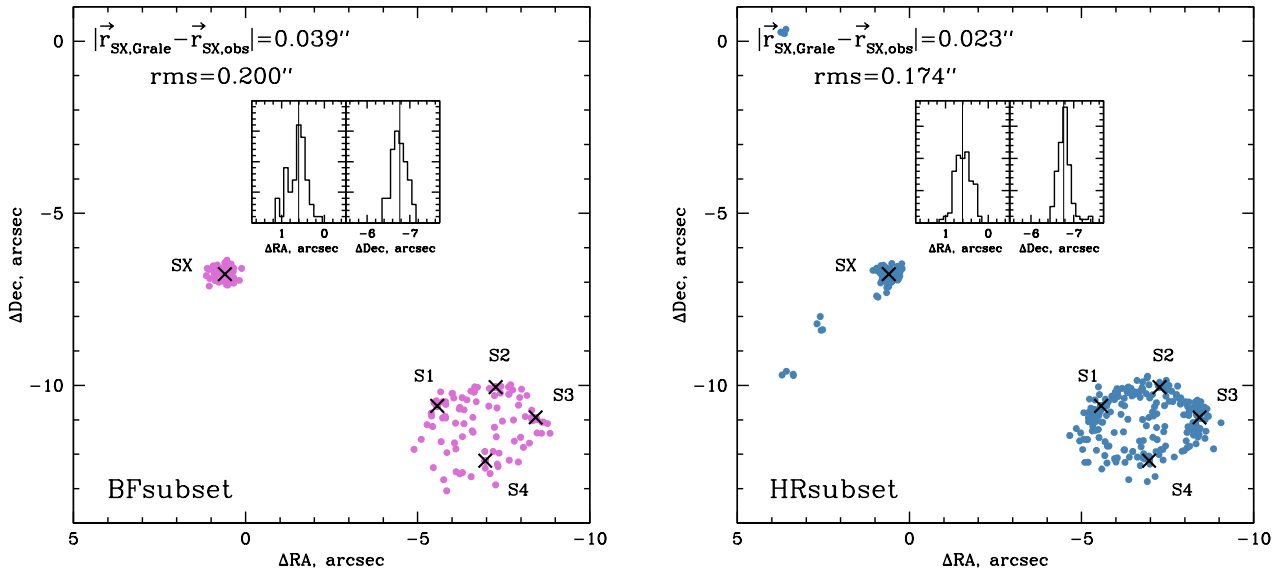


Figure 3. Of the 75 runs, we selected those that have no GRALE predicted images between the two black dotted circles centered on the S1-S4 quad, with radii of $2.5''$ and $7''$, and shown in Figure 2. This selection leaves 17 BestFitness (*left*) and 28 HighResolution (*right*) maps. For the BestFitness maps (*left*) the displacement between the observed and predicted SX, and rms of the scatter of predicted positions are $0.039''$, and $0.200''$, respectively. The corresponding values for the HighResolution (*right*) maps are, $0.023''$, and $0.174''$. The insets in both panels show the distribution of the ΔRA and ΔDec of predicted SX images. Vertical lines mark the observed values.

seed, so the runs are independent. Some runs slightly vary the number of Plummets, as well as the center and size of the reconstruction grid.

In each of the 75 runs we identify two solutions and the corresponding mass maps. (1) The first is the solution that has the best fitness of all the 9 sequential solutions. For *MACS J1149* runs, these are usually the 4th, 5th or 6th solution in a specific run. We call these the *BestFitness* reconstructions, or maps. (2) The second solution is identified from the two last solutions—8th and 9th—as the one with the better fitness. We call these the *HighResolution* maps, because latter solutions have finer grids and more Plummets making up the total mass map, which implies higher mass resolution. Higher resolution will be advantageous in *MACS J1149* because it hosts many closely spaced images in the vicinity of Refsdal’s quad S1-S4. Selections (1) and (2) yield 75 maps each. (In 6 of the 75 runs, the *BestFitness* and the *HighResolution* maps are the same, so the total number of unique maps is 144, instead of 150. Because this is a small fraction of the total, we do not eliminate the redundant maps.)

In addition to the *BestFitness* and *HighResolution* sets of maps, we also analyze one subset from each of these: we call these *BFsubset* and *HRsubset*, respectively. These maps are selected based on how well they reproduce images S1-S4 (see Section 3 for details). In all, we have 4 sets of reconstructions, *BestFitness*, *HighResolution*, *BFsubset* and *HRsubset*.

3 IMAGE PLANE PREDICTIONS

The left and right panels of Figure 2 show the distribution of all *GRALE* predicted images of Refsdal for the *BestFitness* and *HighResolution* reconstructions, respectively. (Images corresponding to SY are outside the box shown, and are not considered in this paper.) These images were obtained as follows. For each of the *GRALE* reconstructions, each of the four observed S1-S4 images was traced back to the source plane, and used as a source to generate lens plane images. Note that not all of these sources produced 4 images of the S1-S4 quad, but all produced at least one image very close to observed SX.

As expected, most of the images are associated with the S1-S4 quad, and the location of SX. The images of the S1-S4 quad are not reproduced very well, most likely because *GRALE* does not have enough spatial resolution, even in *HighResolution* maps. The total number of images in each of the two panels is over one thousand. (In principle, each of the backprojected images of the quad should generate 5 images, and the SX image, for a total of 1800 images.) There are also a handful of images far from S1-S4 and SX; these are most likely spurious, i.e. have no observed counterpart. Also as expected, *HighResolution* has more spurious images than *BestFitness*.

The right panel of Figure 2 has a few predicted images in the upper right, scattered widely around $(-8, 3)$. These could be the fourth image of the cluster-wide Refsdal quad, with the fifth image hidden in the BCG. However, only a small fraction of our reconstructions have these images, and none of these remain in Figure 3. We conclude that it is most likely that the SY, S1-S4, and SX comprise a naked cusp, triple-

Model	$\langle r_{\text{SX,obs}} - r_{\text{SX,Gralle}} \rangle$	rms
BestFitness - all 75 maps	0.024''	0.310''
BFsubset - subset of 17 maps	0.039''	0.200''
HighResolution - all 75 maps	0.060''	0.355''
HRsubset - subset of 28 maps	0.023''	0.174''

Table 1. Summary of the four sets of reconstructions discussed in the paper. For each set we quote how well it reproduces the position of Refsdal image SX, which was not part of *GRALE* input. The selection of the maps in the second and fourth row is described in Section 3.

image system split by the cluster. There are no additional images of Refsdal due to the cluster-wide potential.

The concentration of predicted images near the location of observed SX is very high, implying that the predicted position of SX is very well localized. The two insets in each of the two panels of Figure 2 show the histograms of ΔRA and ΔDec of predicted images around the observed SX, whose position is indicated by the vertical lines. To obtain the average coordinates of the predicted position, we include only the images within the $r = 2''$ radius from the observed position, shown as a black dotted circle. This eliminates most spurious images. Note that using the observed SX in this way does not bias the estimation of *GRALE* predicted position, because the displacement between the mean predicted and observed SX position, 0.024'' and 0.060'' for the *BestFitness* and *HighResolution* reconstructions, and the rms, 0.310'' and 0.355'', are small by comparison. These values are displayed in the figure, as well as in Table 1.

The reconstructions that go into the *BFsubset* and *HRsubset* were selected based on how well they reproduce S1-S4 (whose positions were known to all groups in Kelly et al. 2016a), using two criteria. (i) Selected maps should not have any Refsdal images between 2.5'' and 7'' from the center of the S1-S4 quad. There are no observed Refsdal images in this annulus, so any model predicted images here are spurious. (ii) Selected maps should have at least one of the S2, S3, or S4 back-projected images predict the location of S1 to within 0.85'', which is half the distance between S1 and its nearest neighbor, S2. This criterion is somewhat loose, however, a stricter condition would eliminate most of our reconstructed maps. (*GRALE*’s limited spatial mass resolution prevents it from fitting these images better).

Figure 3 is similar to Figure 2, but for the *BFsubset* and *HRsubset*. Even though no cuts other than the two discussed above were imposed, *BFsubset* reconstructions have no spurious images, while the only remaining spurious images in the *HRsubset* are quite far from the observed SX.

The displacement between observed and predicted SX in our 4 sets ($< 0.06''$; see Table 1) appear to be smaller than in most other existing models ($\sim 0.1 - 0.3''$). The smallest published offset is that for the Grillo et al. (2016) model, and is $\sim 0.045''$. Our rms values are in the range 0.17''–0.36'', while other models have rms values between 0.26'' and 0.9''.

Before we leave the image plane, let us look at the critical curve, for Refsdal’s z_s . Figure 4 shows the critical curves for *BestFitness* (thin pink), *HighResolution* (thin blue), *BFsubset* (thick pink), and *HRsubset* (thick blue) curves, and

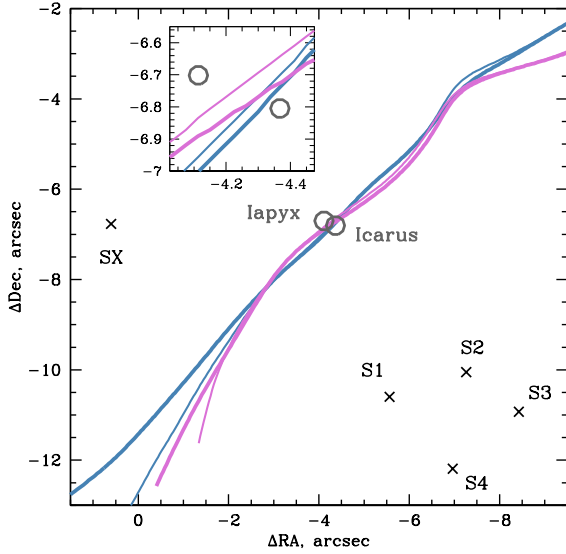


Figure 4. Cluster critical curve in the vicinity of Refsdal images, which are marked with black crosses. Gray empty circles are the Icarus and Iapyx locations, and were not used in GRALE reconstructions. (S1-S4 were used, but SX was not used.) The thin pink and blue critical curves are based on the average of 75 Best-Fitness and 75 HighResolution GRALE maps. The thick pink and blue curves are based on the 17 (28) maps of BFsubset and HRsubset reconstructions. The inset shows a zoomed in region around the transients.

a zoom in the inset. Observed positions of Icarus and Iapyx were not used as model inputs, and yet the GRALE critical curves go between them. Near the transients, the largest separation between the 4 curves is $\sim 0.1''$, while the BFsubset and HRsubset curves are separated by $\sim 0.05''$. By comparison, the separation between the four models presented in Kelly et al. (2018) (namely, Jauzac et al. 2016; Kawamata et al. 2016; Zitrin et al. 2015; Keeton 2010) is $\sim 0.25''$. Furthermore, all GRALE critical curves pass between the two transients, implying that Icarus and Iapyx are counterimages of the same source. Two of the published models (Jauzac et al. 2016; Kawamata et al. 2016) make a similar prediction, while the other two models have both the transients to the North East of the critical curves.

4 GRALE TIME DELAY PREDICTIONS

In the previous section we saw that using only the image positions GRALE is able to predict the position of SX and the locus of the critical curve in the vicinity of the transient, accurately and precisely. In this section we examine how well image positions can constrain H_0 , assuming the observed time delay between Refsdal’s two images SX and S1 is known exactly.

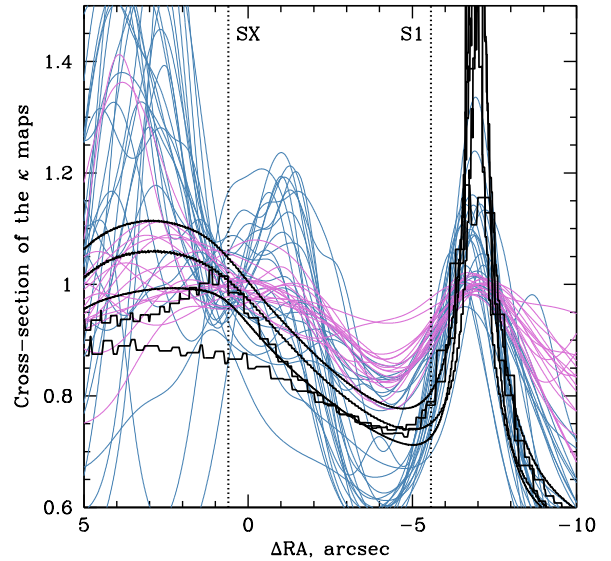


Figure 5. Cross-section of the κ density map taken along the line connecting GRALE predicted positions of SX, and S1. The line is parametrized by the x -coordinate, ΔRA , from the center of the cluster. The two vertical black dotted lines show the positions of the observed SX and S1. The pink and blue curves show the 17 BFsubset and 28 HRsubset reconstructions, respectively. The black curves show all five of the latest (v3 and v4) publicly available (<https://archive.stsci.edu/prepds/frontier/lensmodels/>) reconstructions; from top to bottom (looking at the left edge of the plot) the models are: Sharon et al., Keeton et al., Glafic team, CATS team, and Diego et al. On the right side of the plot most of these models are indistinguishable.

4.1 Generalized mass sheet and monopole degeneracies

It is well known that the mass sheet degeneracy (MSD; Falco et al. 1985), also known as the steepness degeneracy (Saha 2000), is one of the lensing degeneracies that needs to be broken to measure H_0 . Two mass maps, $\kappa_a(\mathbf{r})$ and $\kappa_b(\mathbf{r})$, are related by an MSD transformation if there exists a constant λ , such that $\kappa_b = \lambda\kappa_a + (1 - \lambda)$, or equivalently, $\Sigma_b = \lambda\Sigma_a + (1 - \lambda)\Sigma_{\text{crit}}$ over the entire lens plane, where Σ is the surface mass density of the lens in physical units. Such a transformation would leave most lens observables—image positions, flux ratios, time delay ratios—unchanged, but will rescale all time delays by λ , thereby scaling the estimated H_0 by λ . Because κ depends on the source redshift, the presence of multiply imaged sources at different redshifts breaks the degeneracy, as no single λ works for all sources.

It was demonstrated in Liesenborgs et al. (2008a) and Liesenborgs & De Rijcke (2012) that a generalized version of the mass sheet degeneracy, gMSD, can be present despite sources at multiple redshifts. For gMSD, the added mass sheet is not simply $(1 - \lambda)\Sigma_{\text{crit}}$. Instead, it is a non-uniform disk, Σ_{gen} , centered on θ_c , with its density profile arranged so that images at different redshifts and different locations θ see the same total enclosed mass as they would with the regular

MSD: $\Sigma_b(\theta) = \lambda \Sigma_a(\theta) + (1 - \lambda) \Sigma_{\text{gen}}(|\theta - \theta_c|)$. In the regions of the lens plane that have images of different redshifts located close to each other, gMSD is suppressed, but not eliminated. Its approximate version, agMSD, that reproduces the image properties not exactly, but within observational uncertainty, presents an even wider range of possible mass models.

MSD and its kin, agMSD, are not the only degeneracies. In this paper we will also focus on the monopole degeneracy, MpD (Saha 2000; Liesenborgs et al. 2008b; Liesenborgs & De Rijcke 2012). In regions of the lens plane with no images, the projected mass distribution can be reshaped in any circularly symmetric fashion, as long as the net mass remains the same, and no extra images are produced. Since any number of such operations, with different centers, radii, and shapes can be performed and superimposed, the monopole degeneracy is very powerful.

An important difference between agMSD and MpD is that agMSD reshapes the lens mass distribution over the whole lens plane, while MpD redistributes mass between images only. The immediate consequence is that agMSD is not necessarily affected by the high density of images in the lens plane (as long as they are at approximately the same redshift), while MpD is suppressed in regions where the density of images is high. Other degeneracies can also be present, for example the source plane transformation (SPT; Schneider & Sluse 2014), which is related to MSD, and also reshapes the mass continuously across the lens plane. For brevity, we will talk about agMSD and MpD only, noting that other degeneracies are also possible.

4.2 Illustrating agMSD and MpD in grale reconstructions

We will demonstrate the presence and effect of agMSD and MpD using our GRALE maps. Figure 5 shows the cross-section of the κ density maps taken along the line connecting GRALE predicted positions of SX, and S1. The line is parametrized by the ΔRA coordinate, with respect to the center of the cluster. The pink curves show the BFsubset maps, while the blue lines show the HRsubset. As expected, all the GRALE curves follow the same general trend, for example, all show the presence of the galaxy at $\Delta\text{RA} \approx -7''$, which creates the S1-S4 quad. But because HighResolution maps have Plummer spheres with smaller widths (i.e., higher spatial resolution), they have a sharper density peak associated with that galaxy.

The five black curves in Figure 5 show publicly available reconstructions: parametric models by Sharon et al., Keeton et al., Glafic team, CATS team, and free-form hybrid model by Diego et al., along a line connecting observed SX and S1 Refsdal images. These models show less dispersion than GRALE because they assume specific functional forms for the mass distributions of the galaxy and cluster components, which eliminate many degenerate mass models. GRALE reconstructions do not have such assumptions, and so GRALE curves show a fuller range of density distributions allowed by the multiple images. The realistic range of mass distributions probably lies somewhere between these two types of models: on one hand, some GRALE models are likely to be astrophysically implausible, but on the other, parametric models are too restrictive, and likely do not account for the complexity of mass distribution in lenses, espe-

cially in merging, far-from-relaxed galaxy clusters, such as MACS J1149.

In Figure 6 the pink curves (left panel) show the Best-Fitness set of all 75 GRALE maps, while the blue curves (right panel) show the HighResolution set of the same 75 GRALE maps. As an illustration of agMSD, we highlight two GRALE maps that are closely related by it. In the left panel of Figure 6, these are κ_1 (thick solid black curve), and κ_2 (thin solid black curve). A third curve (thick dashed black) shows $\lambda \kappa_1 + (1 - \lambda)$, with $\lambda = 0.73$, i.e., an MSD-transformed κ_1 cross-section. The cross-sections of these two maps (thin solid and thick dashed) are very similar, but not the same, implying that other degeneracies, such as MpD, are contributing in addition to agMSD. In the right panel, the two agMSD related mass maps are κ_3 (thick solid black curve), and κ_4 (thin solid black curve), and the corresponding factor is $\lambda = 0.55$.

To demonstrate the presence of MpD we first approximately take out the standard MSD, as follows. For every one of the κ cross-sections presented in Figure 6, we find λ such that the curve $\lambda \kappa + (1 - \lambda)$ attains $\kappa = 0$ at some location within the ΔRA range shown in the figure. The resulting κ cross-sections are shown in Figure 7. Though the maps attain $\kappa = 0$ at different locations, for the vast majority it happens within a narrow interval $-0.5'' < \Delta\text{RA} < -0.3''$. The bar code at the bottom indicates the locations of multiple images within $\pm 6''$ of the SX-S1 line, mapped on to the ΔRA axis. The $\pm 6''$ range includes all but 4 of the knots of the spiral galaxy at $z = 1.489$; more distant multiple images have lesser influence on the mass distribution near SX and the Refsdal quad. Because the bulk of the images in this region are knots of the same spiral galaxy, most of the agMSD is just the standard MSD and its approximate versions, arising due to small uncertainties in the image positions.

If the maps were related by agMSD transformations, all the curves would be nearly identical (in the case of pure MSD they would be identical). To judge the importance of agMSD one must compare the corresponding panels of Figures 6 and 7. The curves on the right side of both panels of Figure 7, at $\Delta\text{RA} \lesssim -2''$, show less dispersion compared to the corresponding panels in Figure 6, implying that agMSD is present in GRALE maps, and was taken out, and that the small residual differences are due to other degeneracies, mostly MpD. At $\Delta\text{RA} \lesssim -2''$ multiple images are abundant, so MpD does not have much room to play out, but is still present.

On the left side of the panels, at $\Delta\text{RA} \gtrsim -2''$, where the images are sparse, MpD becomes more important, diminishing the visibility of MSD, and making the density cross-sections have different shapes. In other words, it is the redistribution of mass between images due to MpD that accounts for most of the scatter in the curves at $\Delta\text{RA} \gtrsim -2''$ in both panels of Figures 6 and 7.

4.3 H_0 from lensed images only

We conclude that both types of degeneracies, agMSD and MpD, contribute to mass maps, and will therefore contribute to the model time delay, τ_{model} , and estimation of H_0 .

Figure 8 shows the cross-section of the arrival time surface along the same straight lines that were used in Figures 6 and 7. On the vertical axis the curves were shifted

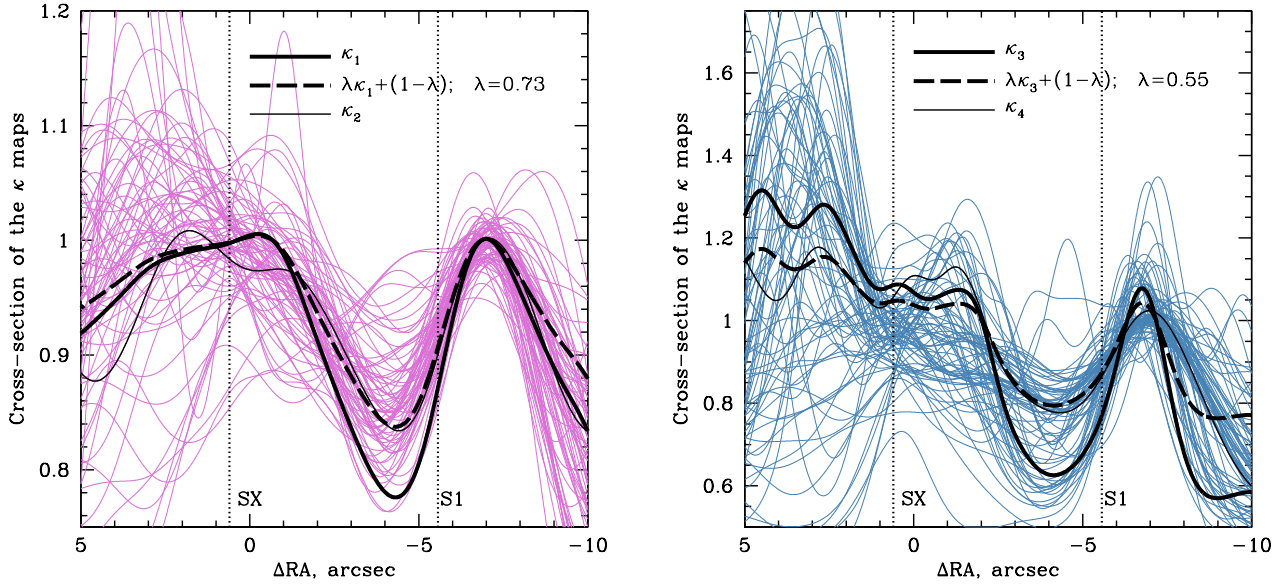


Figure 6. Similar to Figure 5. *Left:* The pink curves show the BestFitness set of all 75 GRALE maps. The thick solid black curve highlights one of these maps (which we call κ_1), while thin solid black curve highlights another map (κ_2). These two are related by approximate, generalized MSD, because $\lambda\kappa_1 + (1-\lambda)$ curve, shown as the thick dashed black curve, is very similar to κ_2 . *Right:* Same, but for the 75 HighResolution maps. Note that the extent of the vertical axes are different in the two panels.

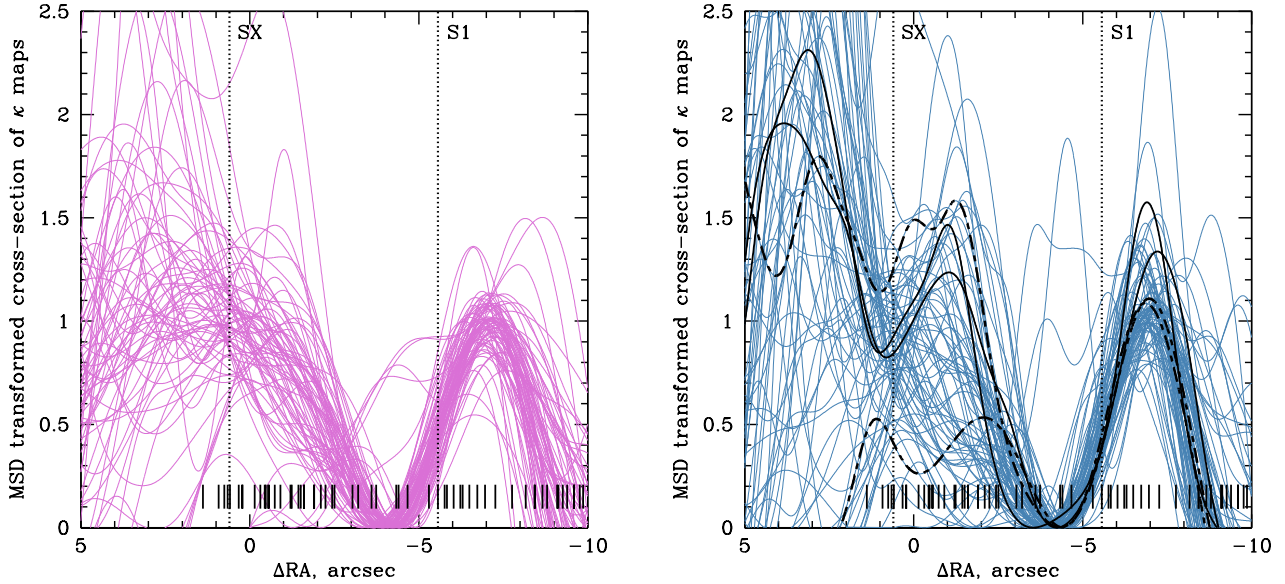


Figure 7. *Left:* Similar to Figure 6, but here we have taken out MSD, so that other degeneracies become visible. To do that, for every one of the 75 BestFitness κ cross-sections presented in the left panel of Figure 6, we find λ such that the curve $\lambda\kappa + (1-\lambda)$ attains $\kappa = 0$ at some location within the ΔRA range shown in the figure. The bar code at the bottom shows the locations of multiple images within $\pm 6''$ from the SX-S1 line, mapped on to the ΔRA axis. *Right:* Same as the left panel, but for HighResolution. The four cross-sections highlighted in black are the reconstructions labeled A, B (solid lines), and C, D (dot-dashed lines) in Figures 9 and 10.

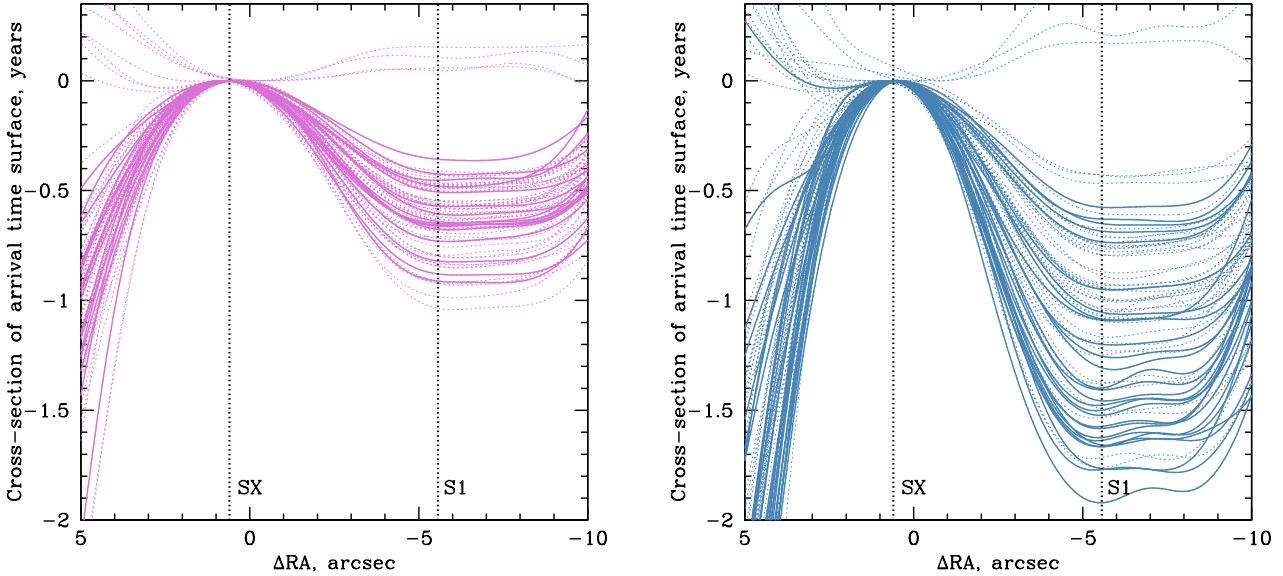


Figure 8. *Left:* Cross-section of the arrival time surface taken along the line connecting GRALE predicted positions of SX, and S1. The line is parametrized by the x -coordinate, ΔRA , from the center of the cluster. The two vertical black dotted lines show the positions of the observed SX and S1. The thin dashed pink curves show the HighResolution set of all 75 GRALE maps. The thick solid pink curves show the BFsubset of 17 maps. *Right:* Same as the left panel, but for the 75 HighResolution maps, and 28 HRsubset maps. The scale is the same in both panels.

to go through zero at the location of predicted SX, to make it easier to read off the model time delay between SX and S1, $\Delta\tau_{\text{model}}$. The dashed curves in both panels show all 75 BestFitness and 75 HighResolution models, while the solid thick curves represent the BFsubset and HRsubset.

The model time delay, $\Delta\tau_{\text{model}}$, and the observed time delay, τ_{obs} , are connected by $\Delta\tau_{\text{obs}} = (H_{0,\text{fid}}/H_0)\Delta\tau_{\text{model}}$, where $H_{0,\text{fid}}$ is the fiducial value of the Hubble constant assumed in GRALE runs. If the observed time delay is known, measuring τ_{model} is equivalent to measuring H_0 . Because of the lensing degeneracies, there is a range of predicted $\Delta\tau_{\text{model}}$ values. Hence, using just the lensed images for mass reconstruction, as GRALE does, leaves one with many degenerate models. $\Delta\tau_{\text{model}}$ values span a factor of 10, from ~ 0.2 to ~ 2 years. Therefore the 123 lensed images that we use, with no additional constraints, can constrain H_0 only to within a factor of 10.

To obtain a competitive measure of H_0 given $\Delta\tau_{\text{obs}}$, one needs to isolate a narrow range of mass models. Though lensing by itself cannot break the degeneracies, it can help us determine what additional information would be helpful. Specifically, lensing mass reconstructions can tell us what observables correlate with $\Delta\tau_{\text{model}}$.

4.4 H_0 from lensed images and galaxy masses

Figure 9 shows that the (projected) mass of the galaxy interior to S1-S4 is correlated with model time delay, $\Delta\tau_{\text{model}}$. The mass is proportional to the difference between the average κ densities within $r \leq 1.5''$ and $r = 2.0'' \rightarrow 2.5''$, where

the latter is assumed to be representative of the projected density of the cluster in the vicinity of the Refsdal quad. We call this quantity $\Delta\kappa_{\text{gal}}$. Because the radii quoted above are the same throughout the analysis, $\Delta\kappa_{\text{gal}}$ is proportional to the mass of the galaxy. The image radius is about $1.5''$, so we are measuring the mass of the galaxy interior to the images.

Note that $\Delta\kappa_{\text{gal}}$ is equivalent to the slope of the density profile of the total (dark matter and galaxy) mass distribution. MSD, which is sometimes called the steepness transformation, changes the slope of the total mass responsible for lensing. The image separation of the S1-S4 quad fixes the total mass enclosed by the four images, but does not say how that mass is partitioned between the galaxy and the cluster's smooth dark matter at that location. Changing that partitioning affects the total density slope. In the rest of the paper we will refer to $\Delta\kappa_{\text{gal}}$ as the galaxy mass, but one must keep in mind that it is analogous to steepness.

We have tried radial ranges other than the ones specified above, but these give the strongest correlation with $\Delta\tau_{\text{model}}$, i.e., the most optimistic scenario. The small symbols in Figure 9 represent the full BestFitness (pink circles) and HighResolution (blue triangles) sets, while the large symbols represent the corresponding BFsubset and HRsubset. All but a small handful of models have SX arriving after S1, as one would expect for the ordering of the saddle and the neighboring minimum, in a naked cusp configuration.

The points in Figure 9 show a well defined trend, with scatter. The main trend is primarily due to agMSD, while the scatter is due to MpD, as well as the approximate nature

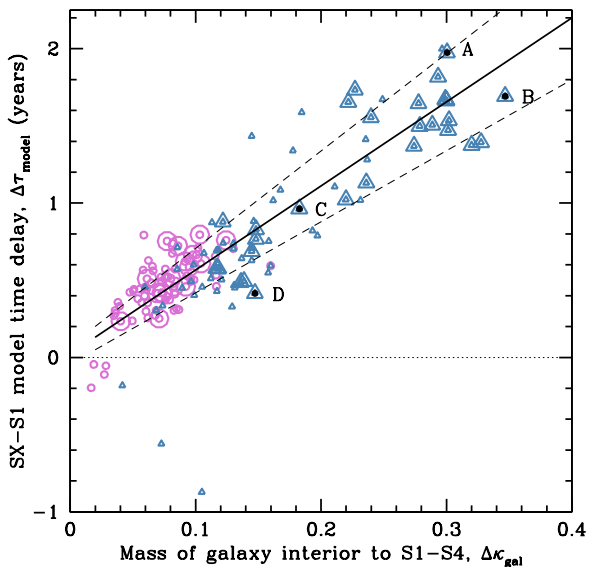


Figure 9. GRALE predicted time delay between SX and S1 (in years) vs. $\Delta\kappa_{\text{gal}}$, which is proportional to the projected central mass of the galaxy interior to the Refsdal quad S1-S4. We measure $\Delta\kappa_{\text{gal}}$ as the difference between the average densities within $r \leq 1.5''$ and $r = 2.0'' \rightarrow 2.5''$, where the latter is assumed to be representative of the projected density of the cluster. The thick black line is the ridge of the trend, while the thin dashed lines enclose approximately 68% of all GRALE models. One σ uncertainty ranges from $\sim 20\%$ for high galaxy masses ($\Delta\kappa_{\text{gal}} = 0.3$), to $\sim 33\%$ for low galaxy masses ($\Delta\kappa_{\text{gal}} = 0.05$). The mass distributions of models A, B, C and D are shown in Figure 10.

of the agMSD, namely that the images are not reproduced exactly. The existence of the trend indicates that an accurate measurement of the mass of the galaxy interior to S1-S4 (which is related to the stellar velocity dispersion) will eliminate most models in Figure 9, and meaningfully constrain H_0 , but the scatter in $\Delta\tau_{\text{model}}$ at a given mass will remain. The thick black line shows the ridge of the trend, while the thin dashed lines enclose approximately 68% of all GRALE models. The fractional uncertainty due to scatter is not constant as a function of galaxy mass; 1σ uncertainty ranges from $\sim 20\%$ for high galaxy masses ($\Delta\kappa_{\text{gal}} = 0.3$ in Figure 9), to $\sim 33\%$ for low galaxy masses ($\Delta\kappa_{\text{gal}} = 0.05$).

Figure 10 gives examples of two high mass (labelled A and B in Figure 9) and two low mass (labelled C and D) galaxies splitting S1-S4. We selected these maps such that the galaxies in each pair had similar masses; in pair A, B (C, D) the two galaxy masses differ by $\sim 20\%$ ($\sim 15\%$). The mass maps were further selected to have their galaxy centers (star symbols) be close to the center of the observed galaxy (black solid dot). In A, B (C, D) the centers are displaced by $\leq 0.09''$ ($\leq 0.24''$). The isodensity contours of these mass distributions are not elliptical, but even isolated ellipticals do not have strictly elliptical isophotes (e.g., Hao et al. 2006; Mitsuda et al. 2017), and presumably isodensity contours.

Parametric models assume fixed functional forms for the cluster and galaxy mass profiles, which artificially suppress MpD, and restrict the shape of the trend due to agMSD.

Thus, under the assumptions inherent in parametric modeling, the plot equivalent to our Figure 9 would look like a single curve, and so most, if not all degeneracies are broken by measuring the mass of the galaxy interior to S1-S4. (This is usually done using a proxy, like the central velocity dispersion.)

Since $\Delta\tau_{\text{model}}$ correlates well with the mass of the galaxy interior to S1-S4, one might ask if a similarly good correlation exists between $\Delta\tau_{\text{model}}$ and the mass of the galaxy, or galaxies, in the close vicinity of SX. Unfortunately, no. This is related to the fact that near S1-S4, agMSD is the dominant degeneracy, and mass distributions connected by it are simple scalings of each other. On the other hand, the main degeneracy near image SX is MpD, and there is no simple relation between the mass maps connected by MpD. So the prevalence of MpD near SX means that nearby galaxy masses will not provide a useful constraint.

Therefore the only galaxy mass that correlates with $\Delta\tau_{\text{model}}$, and hence is useful for constraining H_0 , is the mass of the galaxy enclosed by S1-S4. If the mass of that galaxy is estimated accurately, and no parametric assumptions are used, H_0 can be estimated to within $20\% - 33\%$, depending on the mass of the galaxy.

4.5 H_0 from lensed images, galaxy masses, and parametric assumptions

The predicted time delay between S1 and SX obtained by parametric models (Jauzac et al., Sharon et al., Oguri et al., Grillo et al., Zitrin et al.) and free-form hybrid models (Diego et al.) are presented in Figure 3 of Kelly et al. (2016a). Most models have $1\sigma \sim 25$ days, or $\sim 7\%$ uncertainty in $\Delta\tau_{\text{model}}$. The transition from $20\% - 33\%$ precision on H_0 to $\sim 7\%$ is accomplished by introducing parametric forms describing the distribution of mass associated with the cluster dark matter, and the individual galaxies in the cluster. Because these priors differ between various lensing inversion methods, some models—even those using the same LENSTOOL software (Kneib et al. 1993; Jullo et al. 2007): Sharon et al. and Jauzac et al.—differ by $2\sigma - 3\sigma$. This is an indication that the parametric assumptions are somewhat too restrictive; in other words, not all of these assumptions can be correct.

An eye-ball estimate of the combination of these models gives an uncertainty of $\sim 18\%$, similar to that obtained through Bayesian analysis from these data, where one finds $H_0 = 64^{+9}_{-11} \text{ km s}^{-1} \text{ Mpc}^{-1}$ (Vega-Ferrero et al. 2018).

4.6 H_0 from lensed images and absolute magnification of SX

Because the absolute fluxes of supernovae Type Ia are standardizable, they allow for precise determination of the magnification at the location of their images, and can in principle be used to break MSD in cluster lenses (Rodney et al. 2015). Though Refsdal is not Type Ia, one can still ask if knowing the magnification will break some existing degeneracies.

Magnification, μ , is related to normalized surface mass density κ , and shear γ , through $\mu = [(1 - \kappa - \gamma)(1 - \kappa + \gamma)]^{-1}$. Because of MSD, model time delay is related to κ , and to μ . Therefore one should expect that $\Delta\tau_{\text{model}}$ between SX and S1

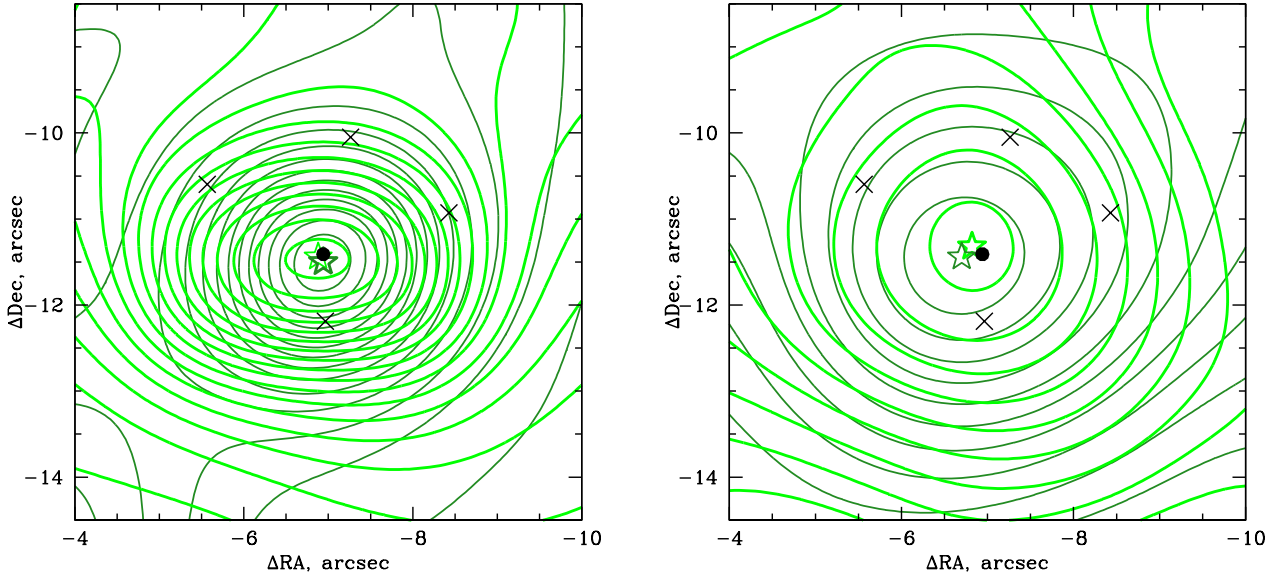


Figure 10. *Left:* Density contours of the total mass distribution of two individual GALE reconstructions, represented by black dots labeled A and B in Figure 9. The two have very similar density profile slopes near the image circle. Contours are linear and are separated by $\delta\kappa = 0.05$. Four black crosses show the locations of S1-S4. The star symbols mark the centers of the two mass peaks, and the black filled circle is the center of the cluster elliptical, which splits images S1-S4. The fractional difference in the predicted H_0 is $\sim 22\%$. *Right:* Same as the left panel, but for the two models labeled C and D. The fractional difference in the predicted H_0 is $\sim 80\%$. The offset between the center of the observed galaxy and the center of the galaxy peak in the two panels ranges from $0.07''$ to $0.24''$. Note that the galaxy interior to S1-S4 was not used in the reconstruction.

is related to μ at SX; this is shown in Figure 11. We will now account for the main trend, through the MSD parameter λ , used in Section 4.2 and Figure 7, where all GALE models have been MSD transformed to have zero mass sheet in the lens plane region between SX and the S1-S4 quad. The GALE reconstructed density (Figure 6) and the density in Figure 7 are related by, $\kappa_{\text{GrALE}} = \lambda\kappa_{\text{Fig.6}} + (1 - \lambda)$. Typical κ at SX in Figure 7 is around 1, with scatter. The black thick curve in Figure 11 is obtained by assuming that $\kappa_{\text{Fig.6}} = 0.9$, γ is related to κ through $\gamma_{\text{GrALE}} = g(1 - \kappa_{\text{GrALE}})$, where $g = 15$, and $\Delta\tau_{\text{model}} \propto l\lambda$, where $l = 3.5$. (Other similar sets of values for $\kappa_{\text{Fig.6}}$, g and l can also reproduce the main trend.) Dashed curves are at $\pm 35\%$ of $\Delta\tau_{\text{model}}$ (solid thick curve), and enclose approximately 68% of all GALE points. This means that knowing the exact magnification at SX translates into uncertainty in λ of $\pm 35\%$, at 1σ level. For a known observed time delay, $H_0 \propto \Delta\tau_{\text{model}}$, and MSD implies that $\Delta\tau_{\text{model}} \propto \lambda$, therefore 1σ uncertainty on derived H_0 is 35%, somewhat larger than what was obtained in Section 4.4 using galaxy mass.

Can one reduce uncertainties on H_0 further by combining observed magnification of SX and observed mass of galaxy enclosing S1-S4? This is unlikely; the scatter in Figures 9 and 11, which is due to MpD, prevents significant reduction in uncertainties. It appears that either galaxy mass, or magnification of SX will reduce uncertainty to approximately the same level.

What about magnification of Refsdal image S1? Since GALE does not accurately predict the location of the quad

images, using GALE predicted magnification—which depends on the second derivative of the lensing potential—is ill advised.

5 SUMMARY AND DISCUSSION

The value of H_0 affects almost every aspect of cosmology, from distance scale to fundamental physics. The goal of this paper was to understand how various constraints affect the uncertainties on H_0 measurement based on cluster lensing.

To separate out the constraints provided by lensed images alone, we used free-form GALE, a lens inversion method that relies solely on image positions. No information about any cluster galaxy was used. GALE predicts very accurately ($\Delta = 0.17'' - 0.36''$) and precisely (rms = $0.023'' - 0.060''$) the position of the cluster-wide saddle point, SX, and the locus of the cluster critical curve ($< 0.1''$), which goes between the transients.

While GALE predictions in the image plane are excellent, the predicted time delays span a very large range, implying that these lensed images alone do not constrain H_0 significantly. This is due to the presence of unbroken degeneracies, mostly the approximate generalized mass sheet degeneracy (agMSD), and the monopole degeneracy (MpD). We showed that their regions of dominance vary across the lens plane. In regions where multiple images at the same redshift are plentiful, agMSD dominates, but MpD is nearly broken. This is well exemplified by the region around Refs-

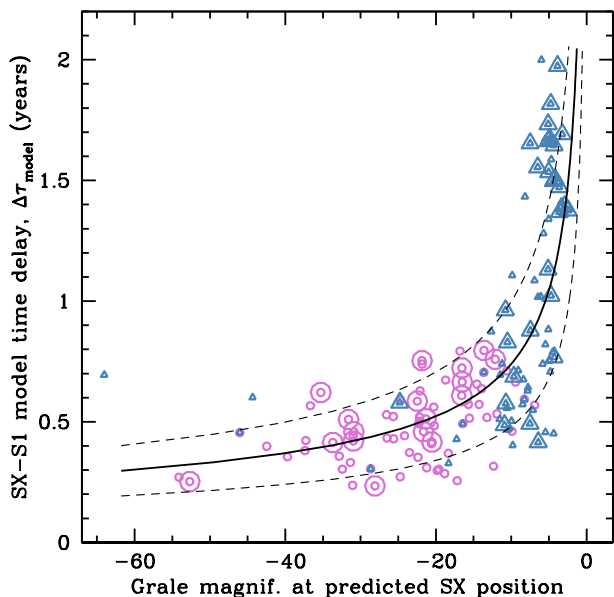


Figure 11. GRALE time delay vs. magnification at the predicted location of SX. (Five points from each of HighResolution and BestFitness sets are outside the limits of the plot.) The black thick curve was obtained using the MSD parameter, λ (Section 4.2 and Figure 7), as discussed in Section 4.6. The thin dashed lines contain approximately 68% of GRALE models. If magnification at SX is known exactly, then the model time delay, and hence H_0 are constrained to $\pm 35\%$, at 1σ .

dal images S1-S4, where multiple knots of the background spiral abound. In the region surrounding SX, images are less plentiful, and there is no equivalent of the S1-S4 quad. Here, both agMSD and MpD play a role, and the large scatter in the shapes of density distributions in this region is due to MpD. Because MpD is relatively suppressed around S1-S4, and agMSD dominates, the mass of the galaxy enclosed by S1-S4 correlates well with the model time delay. Thus, measuring this galaxy’s mass would effectively break agMSD, leaving just the scatter due to MpD.

We conclude that using the currently available data, the multiple images by themselves limit the range of allowable $\Delta\tau_{\text{model}}$ to 0.2–2 years, or $\sim 1000\%$ uncertainty in H_0 . Obviously, additional constraints are needed. We showed that the mass of the galaxy splitting S1-S4 quad correlates well with GRALE model time delay, which is proportional to H_0 . Including an accurate estimate of the galaxy mass would cut down on the range of mass models, and reduce uncertainties to 20%–33% (at 1σ), or potentially better, if image positions are reproduced very well. Absolute magnification of image SX also correlates with model time delay; its measurement would yield 35% uncertainties at 1σ . However, combining galaxy mass and magnification information is unlikely to improve precision significantly because the main remaining degeneracy is MpD, whose contribution to the mass distribution in the lens plane is ‘stochastic’ and cannot be described by a scaling relation.

Uncertainties smaller than 20%–35%, of order a few percent, are a consequence of imposing assumptions on the

shapes of the galaxy and cluster mass distributions. An interesting future exercise with GRALE would be to determine what density of images would be required to suppress MpD sufficiently, to achieve a measurement of H_0 with a few percent precision.

We propose that a reliable estimate of H_0 from Refsdal can be obtained by exploiting the advantages of two types of lensing inversion techniques: parametric, and free-form methods, like GRALE, that are capable of exploring a wide range of mass models. The advantage of parametric methods is that their models incorporate our knowledge about average galaxy and cluster properties, while the advantage of GRALE and similar methods, is that they recognize that averages might not be applicable, especially in a highly non-equilibrium environment of a merging cluster like MACS J1149.

Carrying out a reliable measurement of H_0 would also require some additional data. It is essential to obtain an accurate estimate of the mass of the galaxy enclosed by S1-S4. Measuring spectroscopic redshifts for all known images will help improve the accuracy of the mass model (Johnson & Sharon 2016; Williams et al. 2017). Any additional images, beyond the current set, will be also welcome.

Given these data, free-form methods would be able to narrow down H_0 to 20%–33% or somewhat better, and, more importantly, provide a conservative estimate of the uncertainties (Priewe et al. 2017). Individual parametric models will yield uncertainties of $< 10\%$, or smaller, but these need not agree with each other. One way to combine the parametric models is by using the Bayesian formalism outlined in Vega-Ferrero et al. (2018), but to weight the models (using q_i parameter in eq. 7) by the lens plane rms before including them in the Bayesian analysis. A low lens plane rms is a necessary, but not a sufficient measure of how well a mass model approximates the true mass distribution. However, it remains the best available measure.

An H_0 measurement can be deemed reliable if GRALE, or similar method, and Bayesian-combined parametric models, yield the same value to less than $\sim 2\sigma$. The combined parametric models would provide the optimistic estimate of uncertainties, while GRALE, or similar, would provide the conservative uncertainties.

ACKNOWLEDGMENTS

The authors are grateful to all the Hubble Frontier Fields modeling teams for providing lensed image data. The authors would like to thank Patrick Kelly for providing useful suggestions that helped improve the paper, and Kevin Sebesta for his help with some data files. The authors acknowledge the Minnesota Supercomputing Institute for their computing time, resources, and support. The background HST image of MACS J1149 in Figure 1 was obtained from <http://hubblesite.org/image/3079/category/12-cosmology>.

REFERENCES

- Bonvin V., Tewes M., Courbin F., Kuntzer T., Sluse D., Meylan G., 2016, *A&A*, **585**, A88
 Bonvin V., et al., 2018, preprint, ([arXiv:1804.09183](https://arxiv.org/abs/1804.09183))

- Brammer G. B., et al., 2016, *ApJS*, **226**, 6
- Courbin F., et al., 2018, *A&A*, **609**, A71
- Diego J. M., et al., 2016, *MNRAS*, **456**, 356
- Ebeling H., Barrett E., Donovan D., Ma C.-J., Edge A. C., van Speybroeck L., 2007, *ApJ*, **661**, L33
- Falco E. E., Gorenstein M. V., Shapiro I. I., 1985, *ApJ*, **289**, L1
- Golovich N., Dawson W. A., Wittman D., Ogreaan G., van Weeren R., Bonafede A., 2016, *ApJ*, **831**, 110
- Grillo C., et al., 2016, *ApJ*, **822**, 78
- Grillo C., et al., 2018, preprint, ([arXiv:1802.01584](https://arxiv.org/abs/1802.01584))
- Hao C. N., Mao S., Deng Z. G., Xia X. Y., Wu H., 2006, *MNRAS*, **370**, 1339
- Jauzac M., et al., 2016, *MNRAS*, **457**, 2029
- Johnson T. L., Sharon K., 2016, *ApJ*, **832**, 82
- Jullo E., Kneib J.-P., Limousin M., Elíasdóttir Á., Marshall P. J., Verdugo T., 2007, *New Journal of Physics*, **9**, 447
- Kawamata R., Oguri M., Ishigaki M., Shimasaku K., Ouchi M., 2016, *ApJ*, **819**, 114
- Keeton C. R., 2010, *General Relativity and Gravitation*, **42**, 2151
- Kelly P. L., et al., 2015, *Science*, **347**, 1123
- Kelly P. L., et al., 2016a, *ApJ*, **819**, L8
- Kelly P. L., et al., 2016b, *ApJ*, **831**, 205
- Kelly P. L., et al., 2018, *Nature Astronomy*, **2**, 334
- Kneib J. P., Mellier Y., Fort B., Mathez G., 1993, *A&A*, **273**, 367
- Liesenborgs J., De Rijcke S., 2012, *MNRAS*, **425**, 1772
- Liesenborgs J., De Rijcke S., Dejonghe H., 2006, *MNRAS*, **367**, 1209
- Liesenborgs J., De Rijcke S., Dejonghe H., Bekaert P., 2007, *MNRAS*, **380**, 1729
- Liesenborgs J., De Rijcke S., Dejonghe H., Bekaert P., 2008a, *MNRAS*, **386**, 307
- Liesenborgs J., De Rijcke S., Dejonghe H., Bekaert P., 2008b, *MNRAS*, **389**, 415
- Meneghetti M., et al., 2017, *MNRAS*, **472**, 3177
- Mitsuda K., Doi M., Morokuma T., Suzuki N., Yasuda N., Perlmutter S., Aldering G., Meyers J., 2017, *ApJ*, **834**, 109
- Mohammed I., Liesenborgs J., Saha P., Williams L. L. R., 2014, *MNRAS*, **439**, 2651
- Ogreaan G. A., et al., 2016, *ApJ*, **819**, 113
- Oguri M., 2015, *MNRAS*, **449**, L86
- Plummer H. C., 1911, *MNRAS*, **71**, 460
- Priewe J., Williams L. L. R., Liesenborgs J., Coe D., Rodney S. A., 2017, *MNRAS*, **465**, 1030
- Quinn Finney E., et al., 2018, preprint, ([arXiv:1806.00698](https://arxiv.org/abs/1806.00698))
- Rau S., Vegetti S., White S. D. M., 2014, *MNRAS*, **443**, 957
- Refsdal S., 1964, *MNRAS*, **128**, 307
- Rodney S. A., et al., 2015, *ApJ*, **811**, 70
- Rodney S. A., et al., 2016, *ApJ*, **820**, 50
- Saha P., 2000, *AJ*, **120**, 1654
- Schneider P., Sluse D., 2014, *A&A*, **564**, A103
- Sharon K., Johnson T. L., 2015, *ApJ*, **800**, L26
- Smith G. P., et al., 2009, *ApJ*, **707**, L163
- Treu T., et al., 2015, *ApJ*, **812**, 114
- Treu T., et al., 2016, *ApJ*, **817**, 60
- Vega-Ferrero J., Diego J. M., Miranda V., Bernstein G. M., 2018, *ApJ*, **853**, L31
- Wang X., et al., 2017, *ApJ*, **837**, 89
- Williams L. L. R., Sebesta K., Liesenborgs J., 2017, preprint, ([arXiv:1711.05265](https://arxiv.org/abs/1711.05265))
- Zitrin A., Broadhurst T., 2009, *ApJ*, **703**, L132
- Zitrin A., et al., 2015, *ApJ*, **801**, 44

This paper has been typeset from a $\text{T}_{\text{E}}\text{X}/\text{L}^{\text{A}}\text{T}_{\text{E}}\text{X}$ file prepared by the author.